PROCEEDINGS OF SCIENCE

Effects of non-continuous inverse Compton cooling in blazars

A. Dmytriiev[a,*] **and M. Böttcher**[a]

[a] *Centre for Space Research, North-West University*
Potchefstroom 2520, South Africa

E-mail: anton.dmytriiev@nwu.ac.za

Flaring states of blazars are ideally suited to study the extreme physics of relativistic outflows. A thorough understanding of particle acceleration and cooling mechanisms operating in blazar jets can be achieved via physical modeling of varying multi-band flaring emission from radio up to γ-ray range. The majority of the numerical codes developed for this task use a simplified continuous-loss description for the inverse Compton particle cooling. Such an approximation is however no longer valid in the Klein-Nishina (KN) regime, as particles suffer large relative jumps in energy. In our study, we explore the importance of non-continuous (discrete) Compton cooling losses and their effect on the blazar electron spectrum and broad-band spectral energy distribution (SED) for typical physical conditions during blazar γ-ray flares. We solve numerically the full transport equation that takes into account large relative jumps in energy, and simulate the time-dependent electron spectrum and SED for the conditions of extreme flares of the Flat Spectrum Radio Quasar (FSRQ) 3C 279. We find that non-continuous cooling can significantly modify the shape of the electron spectrum, resulting in notable differences of up to a factor of 1.35 – 2 in the corresponding SEDs during both low and flaring states.

38th International Cosmic Ray Conference (ICRC2023)
26 July - 3 August, 2023
Nagoya, Japan

*Speaker

PoS(ICRC2023)645

1. Introduction

Blazars, a class of jetted Active Galactic Nuclei (AGN) with the relativistic jets closely aligned with the line of sight to the Earth, provide valuable insights into the intricate physics of relativistic outflows. These astrophysical objects exhibit remarkable flux variability across the entire electromagnetic spectrum, including flaring activity on short time-scales ($t_{\rm var} \lesssim 1$ week). Despite extensive research, the origin of blazar flaring behavior remains elusive. A crucial tool for unraveling the complex processes occurring during blazar outbursts is the physical modeling of their multi-band emission. Blazars exhibit a distinctive two-bump spectral energy distribution (SED), with a low-energy bump peaking in the IR/optical/UV/X-ray band and a high-energy bump in the γ-ray range. Flat Spectrum Radio Quasars (FSRQs), a subclass of blazars, are characterized by a pronounced γ-ray dominance. In the leptonic scenario, the dominant γ-ray emission mechanism in FSRQs is inverse Compton (IC) scattering of external photons originating from the broad line region (BLR), accretion disk, or dusty torus (DT) (e.g. [1]).

The modeling of blazar flaring activity is typically conducted within the kinetic framework (e.g. [2]), accounting for processes such as particle injection, acceleration, and cooling within the γ-ray production zone of the blazar jet. In FSRQs, of particular importance are the radiative IC cooling losses, which play a significant role during intense γ-ray flares. When the IC process occurs in the Thomson regime ($\gamma x \ll 1$, where γ is the electron Lorentz factor and $x = \epsilon'_{\rm s}/(m_e c^2)$ is the dimensionless energy of the seed photon), electrons lose only a small fraction of their energy, and the cooling process can be approximated as continuous in the kinetic description. However, in the Klein-Nishina (KN) regime ($\gamma x \sim 1$), electrons lose a substantial fraction of their energy in a single interaction, and the continuous-loss approximation is not valid. Despite this, many existing models still rely on the continuous-loss approximation for IC cooling (e.g. [3, 4]), neglecting/overlooking the non-continuous (discrete) cooling effects. This may result in inaccuracies for certain scenarios.

In our study, we investigate the importance of non-continuous IC cooling effects in FSRQs, where these effects are expected to be particularly pronounced. By revisiting the full transport equation accounting for the discrete nature of energy losses, we aim to examine the deviations from the continuous-loss approximation and explore the impact of discrete jumps of electrons in energy on the electron spectrum and associated emission during strong flaring states of FSRQs.

2. Kinetic framework and numerical approach

2.1 General time-dependent model

We focus on a leptonic emission scenario, where the observed blazar multi-frequency emission is generated by electron-positron plasma in the jet. For simplicity, we will refer to both electrons and positrons as electrons throughout our analysis. In this scenario, the γ-ray emission is generated through the IC process, and as a result, the electrons undergo IC cooling. The evolution of the electron spectrum $N_e(\gamma, t)$ within the blazar emitting zone (a "blob"), considering particle injection, escape, and cooling, can be described by the standard form of the kinetic (Fokker-Planck) equation. This equation, commonly used in the literature, treats cooling as a continuous process and is expressed as follows (e.g. [2]):

$$\frac{\partial N_e(\gamma,t)}{\partial t} = \frac{\partial}{\partial \gamma}\left[-\dot{\gamma}_{\rm cool} N_e(\gamma,t)\right] - \frac{N_e(\gamma,t)}{t_{\rm esc}} + Q_{\rm inj}(\gamma,t), \tag{1}$$

where $t_{\rm esc}$ is the escape time-scale of particles from the emitting zone, $Q_{\rm inj}(\gamma,t)$ denotes the particle injection spectrum, and $\dot{\gamma}_{\rm cool}$ represents the continuous cooling rate, which is a combination of synchrotron and IC cooling rates, $\dot{\gamma}_{\rm cool,syn}$ and $\dot{\gamma}_{\rm cool,IC}$ respectively. The synchrotron cooling rate is given by $\dot{\gamma}_{\rm cool,syn} = -(4\sigma_{\rm T} U_B \gamma^2)/(3 m_e c)$, with $U_B = B^2/(8\pi)$ being the energy density of magnetic field, $\sigma_{\rm T}$ the Thomson cross-section, m_e the electron rest mass, and c is the speed of light. The IC cooling rate, denoted as $\dot{\gamma}_{\rm cool,IC}$, is typically approximated using a continuous-loss formulation derived by [4]:

$$\dot{\gamma}_{\rm cool,IC} = -\frac{4\sigma_{\rm T}}{3 m_e c}\gamma^2 \int_{x_{\rm min}}^{x_{\rm max}} f_{\rm KN}(4\gamma x) u'_{\rm rad}(x) dx \tag{2}$$

$$f_{\rm KN}(z) = \begin{cases} (1+z)^{-1.5}, & \text{for } z < 10^4 \\ \frac{9}{2z^2}(\ln(z) - \frac{11}{6}), & \text{for } z \geq 10^4 \end{cases} \tag{3}$$

where $u'_{\rm rad}(x)$ is the energy density of the seed photon field per unit of photon energy interval (with both $u'_{\rm rad}(x)$ and x as measured in the frame of the blob). While this approximation attempts to reasonably account for KN effects, such as the decrease in cross-section with increasing energy of the seed photon in KN regime, it fails to accurately capture the significant discrete energy jumps experienced by particles. The full transport equation, which properly treats these energy jumps, can be expressed by [5]:

$$\frac{\partial N_e(\gamma,t)}{\partial t} = -N_e(\gamma,t)\int_1^{\gamma} C(\gamma,\gamma')d\gamma' + \int_{\gamma}^{\infty} N(\gamma',t) C(\gamma',\gamma) d\gamma' + \\ + \frac{\partial}{\partial \gamma}\left[-\dot{\gamma}_{\rm cool,syn} N_e(\gamma,t)\right] - \frac{N_e(\gamma,t)}{t_{\rm esc}} + Q_{\rm inj}(\gamma,t) \tag{4}$$

where

$$C(\gamma,\gamma') = \int_{E_*/\gamma}^{\infty} dx\, n'_0(x)\, \frac{3\sigma_{\rm T} c}{4E\gamma}\left[r + (2-r)\frac{E_*}{E} - 2\left(\frac{E_*}{E}\right)^2 - \frac{2E_*}{E}\ln\frac{E}{E_*}\right] \tag{5}$$

is the Compton kernel by [6], which quantifies the rate at which electrons transition from γ to γ', $n'_0(x)$ denotes the number density of the seed photons (per unit of photon energy interval) in the frame of the blob and

$$E = \gamma x\,, \quad E_* = \frac{1}{4}(\gamma/\gamma' - 1)\,, \quad E > E_*\,, \quad r = \frac{1}{2}(\gamma/\gamma' + \gamma'/\gamma) \tag{6}$$

2.2 Numerical code

To numerically solve the full transport equation (Eq. 4), we extend the existing code `EMBLEM` developed by [7]. The code utilizes the Chang & Cooper numerical scheme [8] for solving the kinetic equation. The Compton kernel, which exhibits a sharp peak around $\gamma \approx \gamma'$, presents a challenge for numerical integration. Following the approach proposed by [5], the integration domain is

divided into three sub-regions to handle this peculiarity. The middle region, characterized by $\gamma/(1+\delta) \leq \gamma' \leq \gamma(1+\delta)$ with $\delta \ll 1$, corresponding to the regime in which electrons suffer only small fractional losses, is treated separately. Consequently, the full IC cooling term is expressed using three distinct terms. The term for the middle region, after certain transformations, can be expressed in a continuous-loss form (same as the first term in the RHS of Eq. 1). The expression for the continuous-loss IC cooling rate associated with this term is integrated analytically over the peculiar Lorentz factor domain to avoid issues with the sharply peaked integrand, which yields [5]:

$$\dot{\gamma}_{\rm CL,IC} \approx -\int_{x_{\rm min}}^{x_{\rm max}} dx\, n'_0(x)\sigma_{\rm T}\gamma c s g^2 \left[\frac{3}{2} + \frac{g}{3} + 2g\ln(g) - \frac{3}{2}g^2 - 9sg\left(\frac{1}{3} + \frac{g}{8} + \frac{g}{2}\ln(g) - \frac{2}{5}g^2\right)\right], \tag{7}$$

with $s = 4x\gamma$, and $g = \min(\delta/s, 1)$. It is important to stress, that the rate $\dot{\gamma}_{\rm CL,IC}$ should not be confused with $\dot{\gamma}_{\rm cool,IC}$ (Eq. 2). While $\dot{\gamma}_{\rm cool,IC}$ endeavors to approximately describe the total IC cooling effect of Eq. 4 within a continuous-loss approach, $\dot{\gamma}_{\rm CL,IC}$ specifically considers only small energy losses experienced by electrons. We perform numerical integration of Eq. 7 over the soft photon energies, and the result is added to the synchrotron cooling rate $\dot{\gamma}_{\rm cool,syn}$ to obtain the total continuous cooling rate. For all our numerical computations, we adopt a fixed value of $\delta = 0.05$.

To adapt the `EMBLEM` code to the full transport equation with two additional integral terms (accounting for the non-continuous IC cooling losses), a transformation is performed to align its terms with the mathematical structure of the standard kinetic equation that the code is designed to solve. The non-continuous cooling terms are numerically computed with the use of the electron spectrum from the previous time step, and treated as a time-dependent source term, directly added to the injection term $Q_{\rm inj}(\gamma)$. This treatment simplifies the integro-differential equation into a standard differential equation suitable for the Chang & Cooper scheme. After solving this differential equation, the obtained updated electron spectrum is used to recalculate the non-continuous integral terms with better accuracy, and the process is iteratively repeated until convergence is reached. We verify each time that the normalizations (total number of particles) are identical between the electron spectra for two different cooling scenarios.

3. Application to 3C 279

In this section, we employ the extended `EMBLEM` code to simulate the electron spectrum and SED during realistic blazar flares, and compare the results obtained from continuous-loss and non-continuous cooling scenarios. Our analysis focuses on the FSRQ 3C 279, a representative source of its class, to investigate the significance of discrete IC cooling losses for the typical physical conditions in this source.

3.1 3C 279: the source of interest

3C 279 ($z = 0.536$), is a widely studied FSRQ known for its intense variability across multiple frequency bands, in particular optical and the γ-ray bands. Numerous observations and campaigns have been dedicated to studying this source (e.g. [9, 10]). Continuous observations of this target have been carried out by the *Fermi* Gamma-ray Space Telescope since 2008. The source has exhibited a range of flaring events with high γ-ray flux and very short flux-doubling time-scales of

$\sim$ hours or even $\sim$ minutes [10, 11]. Various modeling efforts suggest that the γ-ray emission from 3C 279 is likely of leptonic origin, with seed photons originating from the BLR and/or dusty torus (e.g. [1, 12]). In our study, we focus on an extreme flare of 3C 279 that occurred in June 2015, characterized by the historically highest γ-ray flux $F_\gamma(0.1-100\,\mathrm{GeV}) \sim 2\times10^{-8}$ erg cm^{-2} s^{-1} and the Compton dominance level $CD \sim 1000$ [13].

3.2 Physical scenario for the quiescent and flaring state

We adopt a one-zone leptonic scenario, where the emission region is represented by a "blob" of radius R_b with a tangled magnetic field B. The blob is moving relativistically along the jet with a Doppler factor δ_b, and is located at a distance r_emz from the central black hole. The blazar high-energy emission is produced within the blob by IC scattering, with the target photon field consisting of synchrotron and an external radiation field, with the latter assumed to be dominated by the BLR photon field (based e.g. on [10, 14]). We approximate the BLR field as a single (Gaussian-shaped) Ly α emission line with a central energy $\epsilon_0 = 10.2$ eV and a width of 0.2 eV (in the AGN frame), which is then transformed it into the frame of the blob (following Eq. 2 in [9]). The BLR luminosity is assumed to be a constant fraction ξ_BLR of the accretion disk luminosity, for which we adopt the value $L_\mathrm{AD} = 0.6\times10^{46}$ erg s^{-1} [10]. We initially model the quiescent state of the source using the multi-band data set from [9], considering it to arise as an asymptotic state of competing injection, cooling and escape [7]. We assume a log-parabola electron injection spectrum above a certain minimum injection Lorentz factor $\gamma_\mathrm{inj,c}$, as well as a particle escape time-scale of $t_\mathrm{esc} \sim 1R_\mathrm{b}/c$.

While we perform a detailed modeling of the quiescent state, our approach to studying the flaring state adopts a more flexible strategy. Instead of conducting a detailed modeling the multi-band data sets of the flare, we simulate a "synthetic" flare that accurately reproduces the observed optical and γ-ray fluxes at the peak of the 3C 279 June 2015 flare. We use the framework by [7], and treat the flaring state as a perturbation of the quiescent state configuration. Based on a study by [13], we assume a scenario where the dramatic γ-ray flux and Compton dominance increase is attributed to simultaneous variations in the Doppler factor and magnetic field.

3.3 Results

We initially employ the model with continuous-loss cooling description by [4] to replicate the observational characteristics of the quiescent and flaring states. We successfully reproduce the data set with our model (see Fig. 1), with the relevant model parameters being listed in Table1. Next, by varying the Doppler factor and magnetic field, we simulate time-dependent electron spectra and SEDs of the flaring state. We set the duration of the flare rise to $2R_\mathrm{b}/c$. As a result, we find the Doppler factor of $\delta_\mathrm{b,fl} = 100$ and magnetic field $B_\mathrm{fl} = 0.3$ G, allowing us to match the two observed fluxes during the peak of June 2015 flare, namely the optical SED flux $\lambda F_{\lambda,\mathrm{opt}}(\lambda = 6000\,\text{Å}) \sim 2\times10^{-11}$ erg cm^{-2} s^{-1}, and the γ-ray flux $F_\gamma(0.1-100\,\mathrm{GeV}) \sim 2\times10^{-8}$ erg cm^{-2} s^{-1} [13]. Considering the obtained Doppler factor, the corresponding rise time-scale of the flare in the observer frame is $t_\mathrm{rise,obs} \approx 0.5$ h. We then repeat the simulations of the quiescent and flaring state with the derived parameters using the full IC cooling description. The comparison of the underlying electron spectra and the SEDs for both quiescent and flaring states is presented in Fig. 1 and Fig. 2 respectively.

Table 1: Parameters of the quiescent state modeling.

B (G)	$R_{\rm b}$ (cm)	$\delta_{\rm b}$	$\gamma_{\rm inj,c}$	$\xi_{\rm BLR}$	$r_{\rm emz}$ (cm)
1.7	2.7×10^{15}	30	130	0.1	6.8×10^{17}

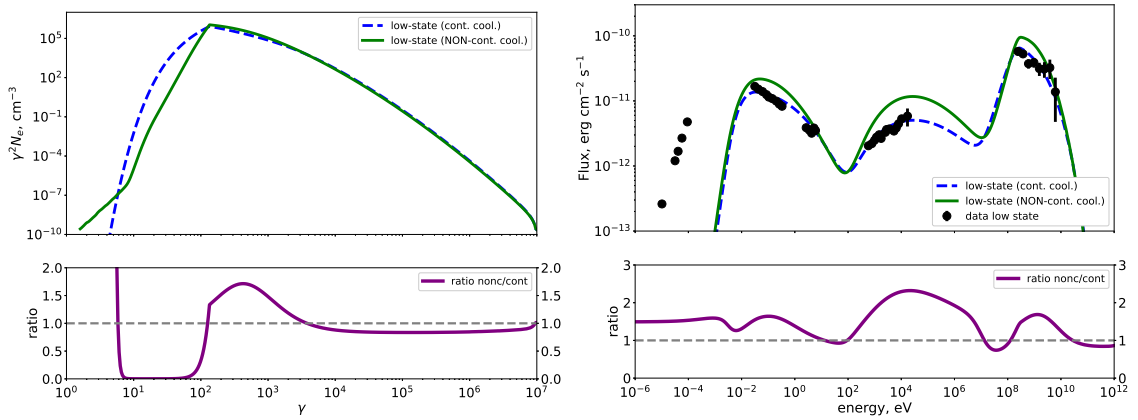

Figure 1: Comparison of the electron spectrum (left) and the SED (right) for continuous-loss approximation (blue dashed) and full non-continuous (solid green) cooling scenarios for the quiescent state of 3C 279. Bottom panels display the ratio of the results obtained for non-continuous cooling to the ones with continuous-loss approximation. Black data points show the multi-band spectral data of 3C 279 in quiescent state by [9].

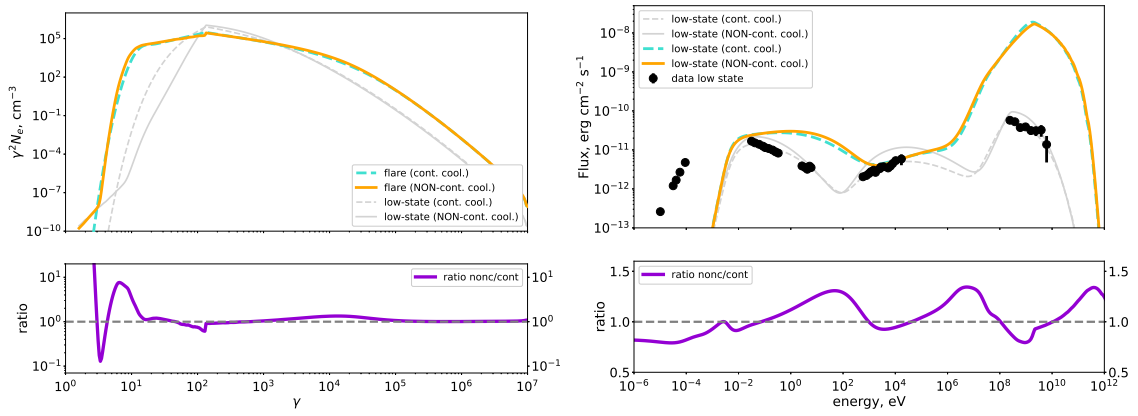

Figure 2: Same as Fig. 1, but for the extreme flaring state of 3C 279. Gray curves represent the quiescent-state electron spectrum and SED, presented for comparison purposes.

4. Discussion

The comparison of the quiescent state results demonstrates overall agreement in the electron spectra beyond the Lorentz factor $\gamma \sim 3 \times 10^3$, with differences of $\leq 10\%$. However, below this Lorentz factor, the deviations become more pronounced. This Lorentz factor coincides with the Klein-Nishina transition for interaction with BLR photons, $\gamma_{\rm KN} \sim (m_e c^2)/(\epsilon_0 \delta_{\rm b})$, and a distinct spectral softening is observed around $\gamma_{\rm KN}$ in the non-continuous cooling case, compared to the continuous-loss one. The deviations then peak at Lorentz factors of $\gamma \sim 400$, corresponding to the cooling break location in the quiescent state, $\gamma_{\rm cool} \sim (3 m_e c^2)/(2\sigma_{\rm T} R_{\rm b} u'_{\rm rad})$. Below $\gamma_{\rm inj,c} = 130$,

corresponding to the cooling-dominated regime where no injection occurs, the deviations become particularly strong, with discrepancies up to several orders of magnitude, indicating poor description of the cooling and of accumulation of cooled particles by the continuous-loss approximation. Additionally, a distinct tail of electrons at very low Lorentz factors is observed in the electron spectrum for the non-continuous cooling case, reflecting the accumulation of electrons that depleted their energy from a single or a few IC interactions. As the discrepancies at Lorentz factors responsible for the majority of the emission are rather large, it leads to a significant impact on the SED, with differences of up to a factor of 1.5 – 2.

In the flaring state, notable deviations in the electron spectra occur at lower Lorentz factors, specifically $\gamma \sim 5 - 100$. A pronounced pile-up of electrons by a factor of ~ 8 is observed around $\gamma \sim 10$, below the cooling break at $\gamma_{\rm cool,fl} \sim 40$, which in the flaring state shifts to a lower position due to an increase in the target photon field density by a factor of $(\delta_{\rm b,fl}/\delta_{\rm b})^2 \sim 10$. A moderate spectral hardening in the electron spectrum for the non-continuous case (compared to the continuous-loss case) is observed around the Lorentz factor corresponding to the Klein-Nishina transition ($\gamma_{\rm KN,fl} \sim 500$). The effect on the SED however appears to be moderate, with discrepancies of up to approximately 35%, as the majority of differences in the electron spectrum occur at Lorentz factors where particle emission is relatively low. Consequently, the impact of non-continuous losses on the SED diminishes as the Doppler factor increases in scenarios where Doppler factor changes primarily drive the flaring activity. A comprehensive exploration of various flare scenarios, including injection increase and re-acceleration, is crucial for a comprehensive understanding of the impact of discrete cooling under diverse physical conditions.

5. Conclusions

In this study, we have explored the significance of non-continuous IC cooling effects in FSRQs, using 3C 279 as a specific case. Our analysis reveals notable deviations in the electron spectra at the Klein-Nishina transition, cooling break location, and in the cooling-dominated regime, leading to distinct features such as spectral hardening/softening, tails and pile-ups. These deviations can have a significant impact on the SED, resulting in differences of approximately 1.35 – 2. However, the influence of discrete IC losses on the SED reduces with increasing Doppler factor, which manifests in scenarios where Doppler factor changes primarily drive the flaring activity. Further exploration of various flare scenarios is necessary to fully understand the implications of discrete cooling under different physical conditions. Overall, our study underlines the importance of considering non-continuous cooling effects in FSRQ modeling.

6. Acknowledgments

The work of M.B. was supported by the South African Research Chairs Initiative of the National Research Foundation[1] and the Department of Science and Innovation of South Africa through SARChI grant no. 64789. A.D. thanks A. Zdziarski, P. Van der Merwe and R. Brose for helpful interactions on various aspects of this study, and acknowledges the FSK-GAMMA-1

[1]Any opinion, finding, and conclusion or recommendation expressed in this material is that of the authors, and the NRF does not accept any liability in this regard.

server facility at the Centre for Space Research which was used for computationally-demanding simulations carried out for this research project.

References

[1] Dermer, C. D., Cerruti, M., Lott, B., et al. 2014, ApJ, 782, 82. doi:10.1088/0004-637X/782/2/82

[2] Chiaberge, M. & Ghisellini, G. 1999, MNRAS, 306, 551. doi:10.1046/j.1365-8711.1999.02538.x

[3] Boettcher, M., Mause, H., & Schlickeiser, R. 1997, A & A, 324, 395. doi:10.48550/arXiv.astro-ph/9604003

[4] Moderski, R., Sikora, M., Coppi, P. S., et al. 2005, MNRAS, 363, 954. doi:10.1111/j.1365-2966.2005.09494.x

[5] Zdziarski, A. A. 1988, ApJ, 335, 786. doi:10.1086/166967

[6] Jones, F. C. 1968, Physical Review, 167, 1159. doi:10.1103/PhysRev.167.1159

[7] Dmytriiev, A., Sol, H., & Zech, A. 2021, MNRAS, 505, 2712. doi:10.1093/mnras/stab1445

[8] Chang, J. S. & Cooper, G. 1970, Journal of Computational Physics, 6, 1. doi:10.1016/0021-9991(70)90001-X

[9] Hayashida, M., Madejski, G. M., Nalewajko, K., et al. 2012, ApJ, 754, 114. doi:10.1088/0004-637X/754/2/114

[10] Hayashida, M., Nalewajko, K., Madejski, G. M., et al. 2015, ApJ, 807, 79. doi:10.1088/0004-637X/807/1/79

[11] Ackermann, M., Anantua, R., Asano, K., et al. 2016, ApJL, 824, L20. doi:10.3847/2041-8205/824/2/L20

[12] Paliya, V. S., Sahayanathan, S., & Stalin, C. S. 2015, ApJ, 803, 15. doi:10.1088/0004-637X/803/1/15

[13] Dmytriiev, A., Böttcher, M., & Machipi, T. O. 2023, ApJ, 949, 28. doi:10.3847/1538-4357/acc57b

[14] Acharyya, A., Chadwick, P. M., & Brown, A. M. 2021, MNRAS, 500, 5297. doi:10.1093/mnras/staa3483